

MEGAPIXEL IMAGE GENERATION WITH STEP-UNROLLED DENOISING AUTOENCODERS

Alex F. McKinney* & Chris G. Willcocks

Department of Computer Science, Durham University, Durham, UK

ABSTRACT

An ongoing trend in generative modelling research has been to push sample resolutions higher whilst simultaneously reducing computational requirements for training and sampling. We aim to push this trend further via the combination of techniques—each component representing the current pinnacle of efficiency in their respective areas. These include vector-quantized GAN (VQ-GAN), a vector-quantization (VQ) model capable of high levels of lossy—but perceptually insignificant—compression; hourglass transformers, a highly scaleable self-attention model; and step-unrolled denoising autoencoders (SUNDAE), a non-autoregressive (NAR) text generative model. Unexpectedly, our method highlights weaknesses in the original formulation of hourglass transformers when applied to multidimensional data. In light of this, we propose modifications to the resampling mechanism, applicable in any task applying hierarchical transformers to multidimensional data. Additionally, we demonstrate the scalability of SUNDAE to long sequence lengths—four times longer than prior work. Our proposed framework scales to high-resolutions (1024×1024) and trains quickly (2-4 days). Crucially, the trained model produces diverse and realistic megapixel samples in approximately 2 seconds on a consumer-grade GPU (GTX 1080Ti). In general, the framework is flexible: supporting an arbitrary number of sampling steps, sample-wise self-stopping, self-correction capabilities, conditional generation, and a NAR formulation that allows for arbitrary inpainting masks. We obtain FID scores of 10.56 on FFHQ256—close to the original VQ-GAN in less than half the sampling steps—and 21.85 on FFHQ1024 in only 100 sampling steps.

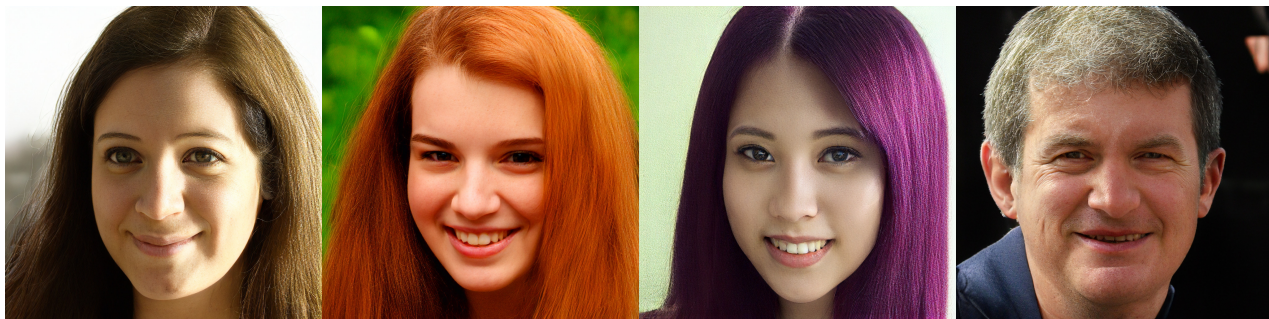


Figure 1: Samples produced using our non-autoregressive approach. Each 1024×1024 sample was generated in ≈ 2 seconds on a GTX 1080Ti—including both discrete latent sampling and subsequent VQ-GAN decoding. At this resolution, autoregressive and (non-adversarial) non-autoregressive models take minutes to sample, or simply do not scale to this resolution.

1 INTRODUCTION

The ideal deep generative model would satisfy three key requirements: high-quality samples, mode coverage resulting in high sample diversity, and computationally inexpensive sampling. Arguably,

*Corresponding Author: alex.f.mckinney@gmail.com

there are other desirable properties such as a meaningful latent space, exact likelihood calculation, and controllable generation. Nonetheless, no current generative model satisfies all three key requirements—let alone additional attractive properties—forming the so-called generative modelling trilemma (Xiao et al., 2021) that dominates modern generative modelling research.

For example, generative adversarial networks (GANs) (Goodfellow et al., 2014) excel at high-quality and fast sampling, but are unstable to train and susceptible to mode collapse (Xiao et al., 2021). Models such as Image Transformer (Parmar et al., 2018), denoising diffusion probabilistic models (DDPMs) (Ho et al., 2020), and score-based models (SBMs) (Song & Ermon, 2019) are stable to train, have mode covering characteristics, and produce high-quality samples. However, they require many network evaluations to produce a single sample. Variational auto-encoders (VAEs) (Kingma & Welling, 2013) permit single step sampling, but fails to produce samples of competitive fidelity. Normalizing flows Dinh et al. (2014) offer exact likelihood calculation, but have a restrictive architecture that makes it parameter inefficient and hard to scale. Vector-quantization (VQ) van den Oord et al. (2017) image models help alleviate computational costs, but mandate a two-stage training scheme and one or more additional models.

This overview of generative modelling demonstrates that no current approach satisfies all three requirements. This motivates research into explicitly addressing this trilemma. In this work, we move towards such a solution, beginning from existing work applying generative models to discrete latents. This provides an excellent starting point in terms of sample quality and mode coverage, but with slow sampling speeds despite operating in a small latent space. We address this by sampling latents using a non-autoregressive (NAR) generative model to close the gap, sampling speed wise, with models such as GANs. Specifically, we use step-unrolled denoising autoencoders (SUN-DAE) (Savinov et al., 2022) to denoise samples from a uniform prior into samples from the discrete latent space defined by a trained vector-quantized GAN (VQ-GAN). We find that SUNDAE is an effective discrete prior over VQ-GAN representations, even on sequence lengths greater than previously evaluated on.

SUNDAE has only previously be applied to language modelling tasks (Savinov et al., 2022) using transformers (Vaswani et al., 2017) to implement their model. Parallel work introduced a drastically more efficient variant—the hourglass transformer (Nawrot et al., 2021)—leveraging a hierarchical architecture targeting language modelling. Though able to be applied to discrete latent modelling, we propose a number of improvements that improve performance on multidimensional data, including modifications to resampling operations and introduction of axial positional embeddings (Su et al., 2021). Though evaluated on discrete latents, the modifications are applicable to any multidimensional data, valuable outside a generative modelling context. Hence, this work further demonstrates the efficacy of hierarchical transformers outside of language tasks.

Given a fast sampling and efficient transformer architecture, we now possess a highly scaleable generative model, with respect to number of layers and spatial resolution of the latent input. Only a minority of the layers are operating at the same resolution as the input, reducing the impact of costly self-attention. Conversely, we cheaply scale the number of layers by adding layers only at the downsampled resolution, allowing for considerably larger models with minor additional cost. To demonstrate this scalability, we train a VQ-GAN operating on 1024×1024 images and apply our framework to the resulting discrete latents. This results in the **synthesis of megapixel images in as few as two seconds** on a consumer-grade GPU. To our knowledge, this is the largest VQ-GAN trained in terms of input size, and the fastest sampling non-adversarial generative framework at this image resolution. This framework includes a number of additional desirable features, such as self-correction, sample-wise self-stopping, conditional generation, and flexible inpainting.

2 RELATED WORK

This work builds upon much prior research into powerful deep generative models, self-supervised representation methods, and efficient transformer architectures, some of which we discuss in this section. For a full review on generative modelling we direct the reader to Bond-Taylor et al. (2021b), and on SUNDAE and hourglass transformers to Savinov et al. (2022) and Nawrot et al. (2021) respectively.

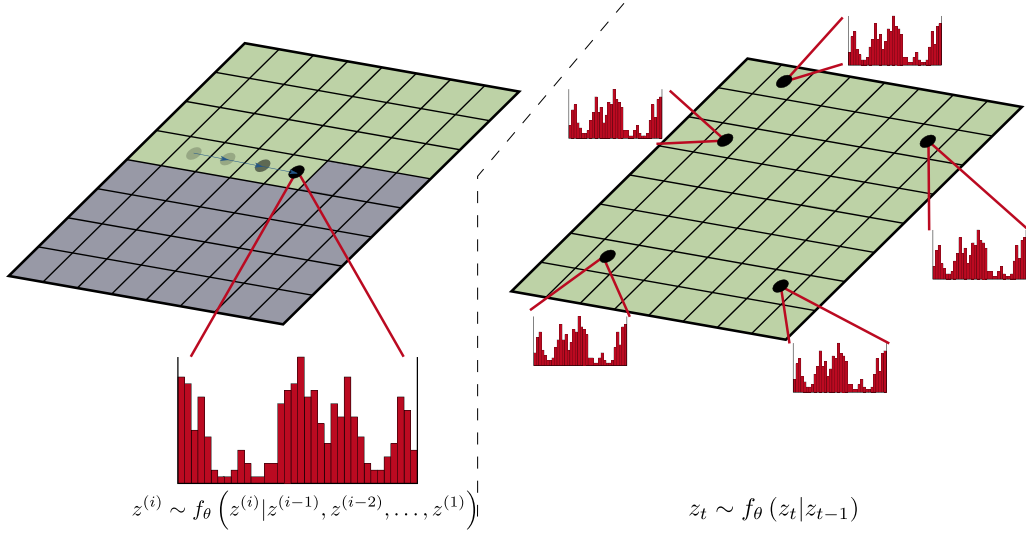


Figure 2: Left: Visualization of autoregressive (AR) sampling. Autoregressive (AR) sampling proceeds one element at a time, meaning the number of sampling steps is equal to the dimensionality of the input and can only make use of past context (indicated by green positions). **Right:** Visualization of non-autoregressive (NAR) sampling. NAR sampling samples an arbitrary number of elements in parallel, allowing for full context and potentially faster sampling.

2.1 AUTOREGRESSIVE GENERATIVE MODELS

One major deep generative model family are autoregressive (AR) models, characterised by a training and inference process based on the probabilistic chain rule. During training, they learn to maximise the likelihood of the data they are trained on, which leads to excellent mode coverage. Prior work using these methods resulted in impressive results in terms of sample quality and diversity, but are ultimately impractical in most real world applications due to their slow sampling speed.

The slow speed is due to their sequential nature, defined by the chain rule of probability. Given an input $\mathbf{x} = \{x_1, x_2, \dots, x_N\}$, an AR model $p_{\theta}(\cdot)$ generates new samples sequentially:

$$p_{\theta}(\mathbf{x}) = p_{\theta}(x_1, \dots, x_N) = \prod_{i=1}^N p_{\theta}(x_i | x_1, \dots, x_{i-1}) \quad (1)$$

meaning that the number of sampling steps is equal to the size of the decomposition of \mathbf{x} , giving an iteration complexity of $\mathcal{O}(N)$.

For certain tasks, the ordering of the decomposition of \mathbf{x} is obvious, for example on text or speech. For images this is less clear, but typically a raster scan ordering is used (Parmar et al., 2018). Certain AR models are order-agnostic (Hoogeboom et al., 2021), allowing for arbitrary ordering to be used during training and inference.

Early examples of AR models include recurrent neural networks (RNNs) and derivatives gated recurrent units (GRUs) (Cho et al., 2014) and long short-term memory recurrent neural networks (LSTMs) (Hochreiter & Schmidhuber, 1997), typically applied to text, audio, and other time series data. Later work introduced models on images, such as PixelRNN and PixelCNN (van den Oord et al., 2016) and PixelSnail (Chen et al., 2017). The introduction of transformer architectures (Vaswani et al., 2017) naturally led to applications in image generation (Parmar et al., 2018), extending even to zero-shot, text-to-image models (Ramesh et al., 2021). In all cases, the iteration complexity is still $\mathcal{O}(N)$, a property intrinsic to AR models.

2.2 NON-AUTOREGRESSIVE GENERATIVE MODELS

Non-autoregressive (NAR) generative models include GANs (Goodfellow et al., 2014), VAEs (Kingma & Welling, 2013), SBMs (Song & Ermon, 2019), DDPMs (Ho et al., 2020), and

flow-based models (Dinh et al., 2014). The number of sampling steps in NAR models is not directly tied to the data dimensionality, however the actual number of steps varies greatly: from single-step generation in GANs and VAEs, to many thousands in early DDPMs and SBMs.

The single-step sampling coupled with high-fidelity results makes GANs the de facto standard for generative models in practical applications. However, GANs are plagued with issues such as unstable training and tendency to collapse onto modes of the target distribution, rather than model the entire target distribution. This is due to not directly optimising for likelihood, but rather using an adversarial loss as a proxy objective. This motivates research into producing other fast-sampling generative models that do not have these issues. Clearly, AR models will never satisfy this requirement due to their $\mathcal{O}(n)$ iteration complexity, leaving improving existing, or creating new, NAR models the only avenue available.

2.3 STEP-UNROLLED DENOISING AUTOENCODER

SUNDAE (Savinov et al., 2022) is a NAR text generative model evaluated on three language modelling tasks: unconditional text-generation, inpainting of Python code, and machine translation—setting a new state-of-the-art among NAR models for the latter. It is capable of fast sampling, producing high quality text samples in as few as 10 steps.

It is trained using a denoising objective, akin to BERT’s objective (Wang & Cho, 2019) but with multiple denoising steps. Given a uniform prior p_0 over some space $Z = \{1, \dots, v\}^N$ where N is the size of the space and v is the vocabulary size, consider the Markov process $\mathbf{z}_t \sim f_\theta(\cdot|\mathbf{z}_{t-1})$ where f_θ is a neural network parameterised by θ , then $\{\mathbf{z}_t\}_t$ forms a Markov chain. This gives a t -step transition function:

$$p_t(\mathbf{z}_t|\mathbf{z}_0) = \sum_{\mathbf{z}_1, \dots, \mathbf{z}_{t-1} \in Z} \prod_{s=1}^t f_\theta(\mathbf{z}_s|\mathbf{z}_{s-1}) \quad (2)$$

and, given a constant number of steps T , our model distribution $p_T(\mathbf{z}_T|\mathbf{z}_0)p_0(\mathbf{z}_0)$ —which is clearly intractable.

Instead, SUNDAE uses an *unrolled denoising* training method that uses a far lower T than is used for sampling. To compensate, they unroll the Markov chain to start from corrupted data produced by a *corruption distribution* $\mathbf{z}_0 \sim q(\cdot|\mathbf{z})$ rather than from the prior p_0 so the model during training sees inputs alike those seen during the full unroll at sample time (Savinov et al., 2022). Typically, $T = 2$ is used during training, as a single step would be similar to BERT’s objective (Devlin et al., 2019) which would not be performant as seen in earlier work using BERT as a random field language model (Wang & Cho, 2019).

The training objective of SUNDAE is the average of all cross-entropy losses on the chain after t steps, which is shown to form an upper bound on the actual negative log-likelihood (Savinov et al., 2022). Increasing T leads to a minor improvement in performance, but slows down training and increases memory usage.

One advantage of this approach is that sampling starts from random tokens, rather than a “masking” token (Bond-Taylor et al., 2021a; Austin et al., 2021). Unmasking approaches means that $T \leq N$ as at minimum, one token is unmasked per step. Additionally, a random prior allows the model to “change its mind” about previously predicted elements during sampling, permitting fine adjustments and correction of errors.

2.4 VECTOR QUANTIZED IMAGE MODELLING

Learning useful latent representations, also known as latent codes, in an unsupervised manner is a key challenge in machine learning. Historically, these representations have been continuous, but in recent work they are often discrete. An early example is vector-quantized VAE (VQ-VAE) (van den Oord et al., 2017), which has three main components: an encoder network, a codebook, and a decoder. The encoder network outputs a compressed continuous representation of the input, and the codebook \mathcal{C} quantizes these representations, outputting discrete indices from 1 to the codebook size v . Each index i maps to one of the codebook embeddings (codewords) e_i . The decoder maps

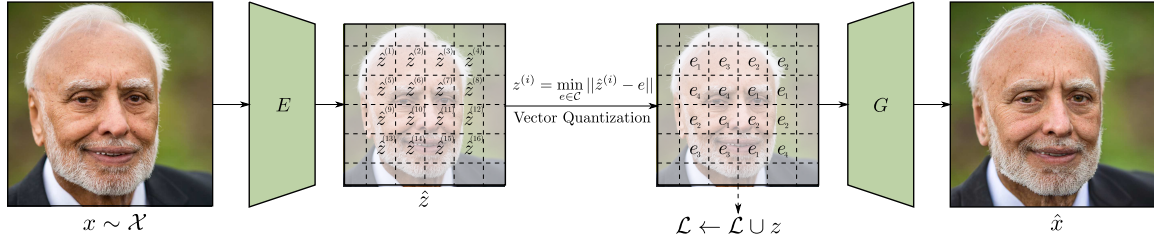


Figure 3: Visualisation of a vector-quantization image model. An encoder model extracts continuous representations from the input. Vector quantization is then used to map each continuous embedding to the closest entry in the codebook, which is then subsequently decoded as a lossy reconstruction of the input. We generate a dataset of latent representations from an image dataset by iterating $\mathbf{x} \in \mathcal{X}$ and appending the resulting discrete representation \mathbf{z} to a set \mathcal{L} .

the quantized embeddings to a lossy reconstruction of the input. VQ-VAE is trained end-to-end to reconstruct the input and to minimize the codebook loss (van den Oord et al., 2017).

Once VQ-VAE is trained, an auxiliary generative model can be trained to generate the discrete latent representations. Using VQ image models helps to alleviate the computational cost in generative models, as they now operate on a smaller latent space, rather than in pixel-space. This is especially significant in AR models due to their $\mathcal{O}(n)$ iteration complexity.

Due to the rate-distortion trade-off, VQ-VAE is not sufficient when the compression rate f becomes large, whilst fixing the codebook size v . VQ-GAN Esser et al. (2021) introduces adversarial and perceptual loss components to VQ-VAE—reformulating the problem as optimising for perceptual quality rather than minimising distortion. This allows for larger f than was possible in prior work before perceptual quality degrades.

2.5 HOURGLASS TRANSFORMERS

Vanilla transformers incur a memory complexity of $\mathcal{O}(N^2)$ for each block (Vaswani et al., 2017), dominated by costly multi-head self-attention mechanisms. The majority of research into efficient transformers focuses on improving the efficiency of the attention mechanisms using sparse attention patterns (Child et al., 2019) or through linear complexity approximations (Xiong et al., 2021).

Recent work has focused on making the architecture itself more efficient. Funnel transformers (Dai et al., 2020) progressively downsamples the input sequence and hence reduces the computational cost of the model. The saved floating point operations (FLOPs) can then be reassigned to create larger models and thus outperform vanilla transformers given the same computational budget. However, the final layer does not operate at the same granularity as the input, making it unusable for tasks such as per-token classification or generative modelling. Hourglass transformers (Nawrot et al., 2021) include both up- and down-sampling mechanisms, resulting in a computational saving whilst being general-purpose models.

3 METHODOLOGY

Our proposed method aims to push the efficiency of generative models to the limit via a combination of current techniques. To do so, we first use pretrained VQ-GANs from Esser et al. (2021) to generate a dataset of discrete latent representations, described in §3.1. By operating at a latent level, we reduce the spatial resolution for our second stage generator. We implement our generator as a modified hourglass transformer, described in §3.2 and trained using a NAR method described in §3.3. This permits extremely fast sampling described in §3.4. To thoroughly test the efficiency and scalability of our approach, we train a megapixel VQ-GAN (described in §3.5) and repeat SUNDAE training and sampling on the resulting discrete latent representations. In §3.6, we explore flexible inpainting using our framework. An overview of training and sampling is shown in Figure 4, and of the latent dataset generation in Figure 3.

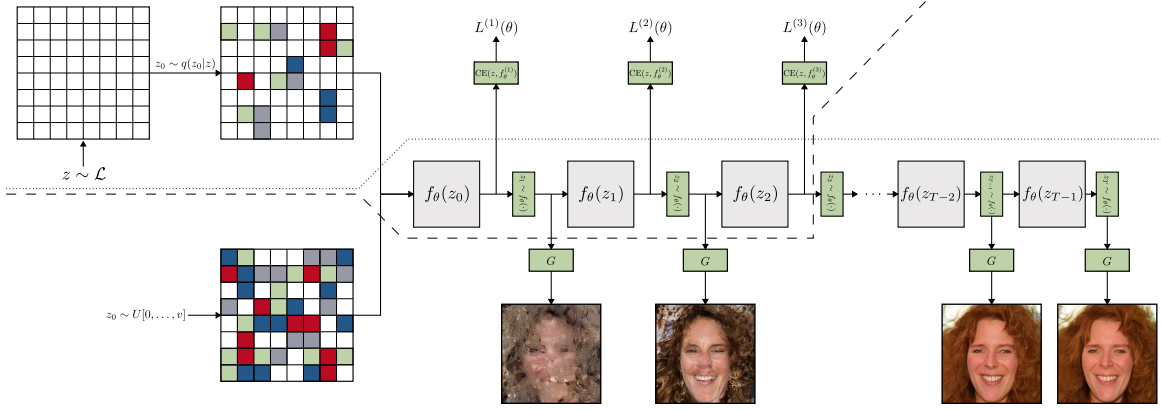


Figure 4: An overview of the SUNDAE training and sampling of discrete latent representations. Above the dashed line shows the training process, whereas below the dotted line shows the sampling process. **Training** begins by sampling $\mathbf{z} \sim \mathcal{L}$ and then sampling from the corruption distribution $\mathbf{z}_0 \sim q(\mathbf{z}_0|\mathbf{z})$. SUNDAE then denoises for 2 to 3 steps, calculating the loss at each step. **Sampling** begins by sampling \mathbf{z}_0 from a uniform prior and denoising for T steps, followed by decoding \mathbf{z}_T to obtain \mathbf{y}_t .

Each component represents the pinnacle of performance in their respective area: compression ratio in VQ image models with VQ-GAN, fast non-autoregressive sampling of discrete data with SUNDAE, and transformer scalability with our modified hourglass transformer. Together, we obtain an extremely efficient generative model that permits sampling at a resolution of 1024×1024 in seconds.

3.1 LATENT DATASET GENERATION

We use the standard two-stage scheme for VQ image modelling (van den Oord et al., 2018) using VQ-GAN (Esser et al., 2021) as our first-stage compression model. For all datasets but FFHQ1024 (see §3.5), we use pretrained VQ-GANs.

The second stage is to train a discrete prior model over the extracted latent representations. To enable this, we generated a latent dataset using a trained VQ-GAN. This allows for faster training of our discrete prior as the latent representations have been precomputed. A downside of this approach is that it limits the amount of data augmentation that can be applied to the dataset. We apply a simple horizontal flip to all images, effectively doubling the dataset size, with no other augmentation. Formally, given a dataset of images \mathcal{X} , a VQ-GAN encoder E with downsample factor f , and VQ codebook \mathcal{C} with number of codewords v , trained on \mathcal{X} , we define our latent dataset \mathcal{L} as:

$$\mathcal{L} = \{\mathcal{C}(E(\mathbf{x})) \mid \mathbf{x} \in \mathcal{X}\} \quad (3)$$

where $\mathbf{x} \in \mathbb{R}^{3 \times H \times W}$ is a single element of the augmented image dataset \mathcal{X} and $\mathbf{z} = \mathcal{C}(E(\mathbf{x})) \in \{1, \dots, v\}^{h \times w}$ is the corresponding discrete latent representation. In other words, each $f \times f$ patch in \mathbf{x} is mapped to a single discrete value from 1 to v (corresponding to a codeword $\mathbf{e} \in \mathcal{C}$), resulting in a latent representation of shape $\frac{H}{f} \times \frac{W}{f} = h \times w$.

We then use \mathcal{L} to train a discrete prior over the latents. Coupled with the VQ-GAN decoder G , we obtain a powerful generative model by first sampling \mathbf{z}_0 from a uniform prior distribution, iteratively denoising using SUNDAE, and then decoding \mathbf{z}_T using the VQ-GAN decoder G to obtain the final sample \mathbf{y} . The training of this discrete prior model forms the bulk of our work in this paper.

3.2 MULTIDIMENSIONAL HOURGLASS TRANSFORMER

Inspired by successes in hierarchical transformers for language modelling (Nawrot et al., 2021), we chose to apply it to the task of discrete latent modelling. Hourglass transformers have been shown to efficiently handle long sequences, outperform existing models using the same computational budget, and meet the same performance as existing models more efficiently by utilising a hierarchical structure (Nawrot et al., 2021). The same benefits should also apply to VQ image modelling.

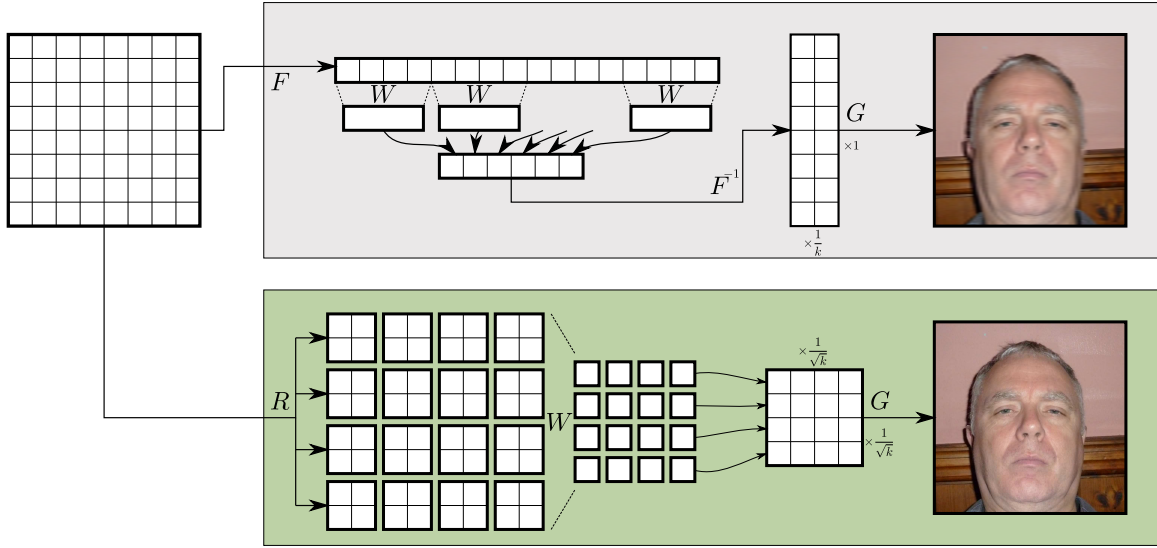


Figure 5: Top: Showing the effect of resampling sequence embeddings using original formulation. Resampling will be applied to only one axis, resulting in resampling in only one axis of the decoded image. **Bottom:** Our method of resampling, extracting two-dimensional patches of size \sqrt{k} , then resampling. The sequence is then flattened and passed to subsequent transformer layers.

However, the design and parameters chosen by the original authors are tailored for language modelling (Nawrot et al., 2021) with limited experiments on image generation (channel-wise downsampling only). We improve upon their architecture for our task of discrete latent modelling, which we believe may also be applicable to multidimensional inputs generally. We leave confirmation of this to future work, and outline modifications in this subsection.

2D-Aware Downsampling—The original formulation of hourglass transformers (Nawrot et al., 2021) introduced up- and down-sampling layers, allowing the use of hierarchical transformers in tasks that have equal input and output sequence lengths. However, we found certain flaws in their original formulation that hinders performance on multidimensional inputs.

In their work, resampling is applied to the flattened embedding sequences, meaning that a corresponding two-dimensional vector-quantized image is resampled more in one axis compared to the other. In their work this was not addressed, as multidimensional experiments were limited to channel-wise sampling with no spatial resampling (Nawrot et al., 2021).

Instead, we reshape the flattened sequence into a two-dimensional form and apply resampling equally in the last two axes. With a resampling rate of k we apply \sqrt{k} in each spatial axis—evenly distributing the resampling among the axes. In our preliminary experiments, this significantly improved the performance of the discrete prior model. A comparison between the previous approach and our amended solution is shown in Figure 5.

For our resampling operations, we use linear resampling (following recommendation by Nawrot et al. (2021) to use linear resampling for image tasks) and a post-resampling attention layer, providing global context and aggregation of information to the resampling operations. Our adjusted resampling method is as follows:

$$h' = A(W^{(\tau)} \cdot R(h) + r), \quad W \in \mathbb{R}^{\frac{(d \cdot h \cdot w)}{k} \times (d \cdot h \cdot w)} \quad (4)$$

where A is the post-resampling attention layer, h is the hidden state of size d , r is the residual (with $r = 0$ when downsampling), R is the modified reshape operation, and W is a learned projection matrix. The reshape operation R was implemented as a space-to-depth operation followed by combining the feature and depth dimensions.

Rotary Positional Embeddings—Transformers have no inductive biases that allow it inherently know the position of an element in the sequence. Embeddings that represent positions must be injected into the model in addition to the input itself. In our work, we choose to use rotary positional embeddings (Su et al., 2021) as they require no additional parameters, incur only a small runtime cost, and can be easily extended to the multidimensional case (Biderman et al., 2021), which we exploit here. Though transformers are clearly capable of learning that elements far apart in a flattened sequence may be semantically close, we found that explicitly extending positional embeddings to the multidimensional case to provide a modest boost in performance and improve the rate of training convergence. The original hourglass transformer on pixel-wise generation also opted to use rotary embeddings (Nawrot et al., 2021) but in the single dimensional case. Though rotary embeddings are agnostic to the self-attention method used, we use full self-attention Vaswani et al. (2017) in all experiments.

Removal of Causal Constraints—In the original AR formulation of hourglass transformers they noted that naively resampling could cause information leakage into future sequence elements—therefore violating the autoregressive property (Nawrot et al., 2021). As our approach is NAR we do not make any special considerations to avoid information leaking into the future. This simplifies the model by avoiding shifting and causal masking operations required in the original work.

3.3 NON-AUTOREGRESSIVE DISCRETE PRIOR TRAINING

We train a SUNDAE model on the flattened (in a raster-scan format) VQ latents $\mathbf{z} = \{\mathbf{z}^{(0)}, \dots, \mathbf{z}^{(N)}\}$ where $N = h \cdot w$. The function $f_\theta(\cdot)$ is implemented using a multidimensional hourglass transformer.

Given a latent $\mathbf{z} \sim \mathcal{L}$, we apply our corruption distribution. This is done by first sampling a corruption threshold vector \mathbf{t} with $t_i \sim U[0, 1]$ and a random matrix \mathbf{R} of the same shape as \mathbf{z} where $R_{i,j} \sim U[0, 1]$. Using this, we construct a mask matrix \mathbf{M} with $M_{i,j} = 1$ when $R_{i,j} < t_i$ and $M_{i,j} = 0$ otherwise. This results in \mathbf{M}_i having approximately t_i of its entries be 1.

Then, given $\mathbf{z}_0 \sim p_0$, we update the \mathbf{z}_0 to start unrolled denoising from:

$$\mathbf{z}_0 \leftarrow \mathbf{M} \cdot \mathbf{z}_0 + (\mathbf{1} - \mathbf{M}) \cdot \mathbf{z}. \quad (5)$$

We then iteratively unroll the current sample \mathbf{z}_{t-1} to obtain \mathbf{z}_t for steps $t \in \{1, \dots, T\}$. To perform one unroll step, simply compute logits $f_\theta(\mathbf{z}_t | \mathbf{z}_{t-1})$ and then sample from the resulting distribution to obtain \mathbf{z}_t , storing the logits at each step t . Then, compute the cross entropy loss between all logits at each t and the target \mathbf{z} . This differs from some NAR solutions which predict the corruption noise ϵ (Ho et al., 2020) rather than the target. The mean of the cross entropy losses is then computed to produce the final loss:

$$L^{(1:T)}(\theta) = \frac{1}{T} \left(L^{(1)}(\theta) + \dots + L^{(T)}(\theta) \right) \quad (6)$$

as in §2.3, which allows for the backpropagation of gradients and consequently the updating of parameters θ , with $T = 2$.

An alternative corruption distribution would be to instead use a deterministic method $\mathbf{z}_0^{(i)} = [\text{MASK}] = v + 1$, essentially replacing all tokens with $M_{i,j} = 1$ with a special masking token. This is similar to “progressive unmasking” of latents used in prior work (Bond-Taylor et al., 2021a). This strategy was not considered as the use of a masking token places an upper bound on T during sampling (updating at most one token per step) as well as not allowing for self-correction, as once a token is unmasked it becomes fixed.

3.4 FAST IMAGE GENERATION

During sampling, we sample $\mathbf{z}_t \sim f_\theta(\mathbf{z}_t | \mathbf{z}_{t-1})$ for a constant number of steps T , beginning randomly from \mathbf{z}_0 sampled from a uniform distribution (Savinov et al., 2022). The original work proposed a number of improved strategies for sampling in a smaller number of steps, including low-temperature sampling and updating a random subset of tokens rather than all simultaneously.

Sampling with a lower temperature, however, reduces the diversity of the outputs. To alleviate this, we anneal the temperature down from a high value (≈ 1.0) down to a low value during the sampling process. We found this retained the fast sampling speed whilst improving diversity.

In certain latent sampling configurations, updating only a small subset of tokens also helps improve diversity. Savinov et al. (2022) used this strategy when performing low-temperature sampling. However, we found that for low-step sampling ($T \leq 50$) that a lower sample proportion meant not all tokens are updated enough, resulting in poor quality samples. Hence, in these cases, we do not follow their proposal and instead use a high sample proportion ($0.5 \sim 0.8$). In scenarios where we are permitted a time-budget allowing for many sampling steps, the sample proportion can be freely reduced for an increase in sample diversity.

If an individual sample does not change between step $t - 1$ and t , it is prevented from being changed further. If all samples are frozen, sampling terminates early, provided a minimum number of steps have been completed. This improves the sampling speed with little cost to the sample quality. This is significant when performing large-batch sampling or when T is large.

Once sampling has terminated, the sampled latent code \mathbf{z}_T is decoded by the VQ-GAN decoder G to produce a final sample \mathbf{y} . In fact, any \mathbf{z}_i in the Markov chain is a valid input to G . Decoding during sampling and visualising \mathbf{y}_t each step t shows the model gradually denoising the latent and correcting errors accumulated during sampling.

3.5 SCALING VQ-GAN TO MEGAPIXEL IMAGES

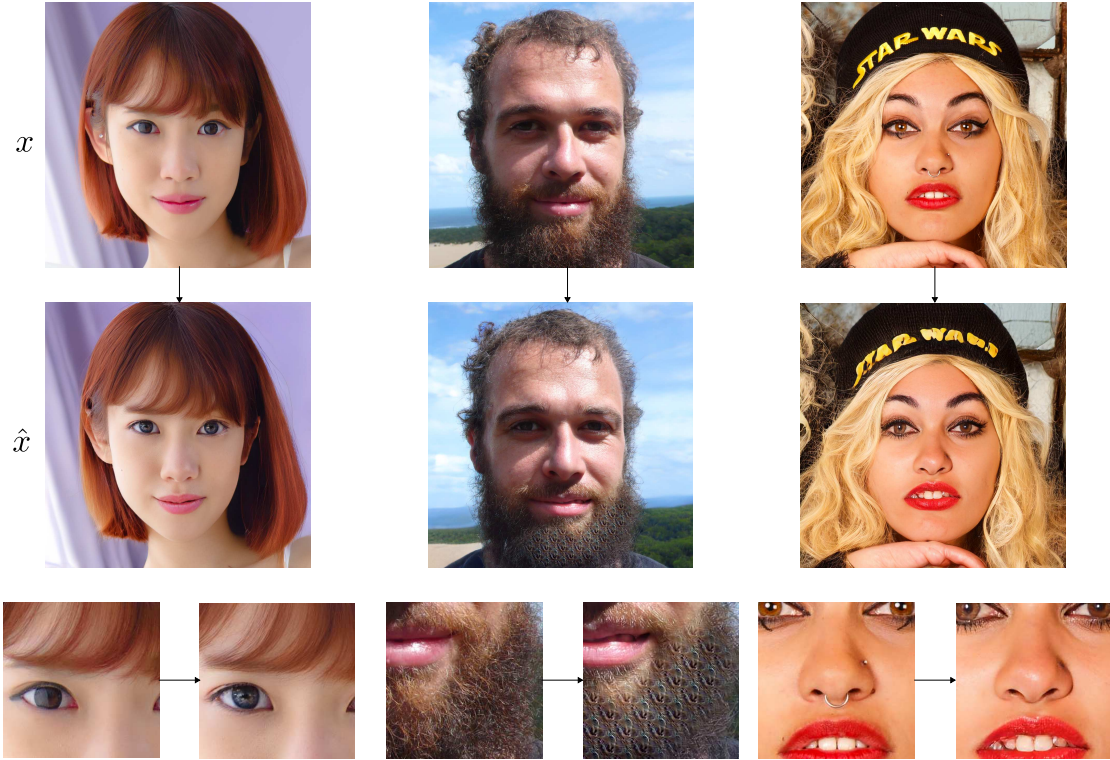


Figure 6: VQ-GAN does not always produce faithful reconstructions due to being optimised for perceptual quality rather minimising distortion. **Left:** The eye colour has been brightened; hair shifted to conceal an ear piercing, rather than reconstruct it. **Middle:** Mode collapse in hair texture; the pose of the lip is altered. **Right:** Text in image is corrupted; nose and lip piercings are removed; eye makeup is altered.

Training at higher resolutions means greater computational requirements and slower sampling speeds. With an AR model, the sampling time can be immense as it scales linearly with data dimensionality, even with an auxiliary VQ image model (Esser et al., 2021). With a NAR model however, the sampling speed is explicitly controlled and does not directly grow as a function of

input size, meaning our proposed generative framework is highly scaleable. To demonstrate this, we applied our proposed framework to megapixel image generation.

We trained a larger variant of VQ-GAN with $v = 8192$ operating on 1024×1024 from FFHQ1024. To our knowledge, this is the highest resolution dataset VQ-GAN has been applied to. Once trained, we generate the latent dataset as before, the only difference being an increased sequence length—greater than SUNDAE was ever tested on in the original work (Savinov et al., 2022). Specifically, we obtain a downsampling rate of $f = 32$, resulting in discrete latents of size $32 \times 32 = 1024$.

The resulting reconstructions are overall of good quality given the large compression ratio in use. However, the reconstructions are not without artifacts. Figure 6 shows examples of particularly prevalent artifacts including occasional unrealistic textures in hair and corruption of text. The corruption of text is a common issue in VQ image models (Ramesh et al., 2021), and the unrealistic textures are likely a result of a lack of model capacity or patch-wise mode collapse.

VQ-GAN is trained to minimise the mean absolute error, perceptual loss, and adversarial loss (Esser et al., 2021) in addition to a k -means VQ loss. Specifically, VQ-GAN is trained to minimise the following loss:

$$\begin{aligned}
L_{\text{PIX}} &= \alpha_{\text{PIX}} \cdot |\mathbf{x} - \hat{\mathbf{x}}| \cdot \\
L_{\text{VQ}} &= \alpha_{\text{VQ}} \cdot (||\hat{\mathbf{z}} - \mathbf{z}||^2 + ||sg[E(x)] - \mathbf{z}||_2^2 + ||E(x) - sg[\mathbf{z}]||_2^2) \\
L_{\text{GAN}} &= \alpha_{\text{GAN}} \cdot (\log D(x) + \log(1 - D(\hat{x}))) \\
\lambda &= \frac{\nabla_{G-1}[L_{\text{PIX}} + L_{\text{PER}}]}{\nabla_{G-1}[L_{\text{GAN}}] + \epsilon} \\
L &= L_{\text{VQ}} + \lambda \cdot L_{\text{GAN}} \\
\alpha_{\text{PIX}} &= 1.0, \alpha_{\text{VQ}} = 1.0, \alpha_{\text{GAN}} = 0.5, \alpha_{\text{PER}} = 1.0
\end{aligned} \tag{7}$$

where $\nabla_{G-1}[\cdot]$ is the gradient with respect to the last layer of the VQ-GAN decoder G and $sg[\cdot]$ is the stop-gradient operator. The generator and discriminator model parameters are updated separately, as is standard procedure in GAN-based literature (Esser et al., 2021).

As there is less relative weight in Equation 7 on minimising distortion, this gives rise to an interesting property of VQ-GAN where the reconstructions may be perceptually valid but distinct from the input. The left reconstruction in Figure 6 demonstrates this with a change in eye colour and a shift in hair position—concealing an ear-piercing. This even more apparent in the right reconstruction where all piercings are flawlessly removed—along with adjustments to eye makeup.

Using VQ image models to compress images further whilst retaining high quality and faithful reconstructions remains an open and challenging area of research—particularly at high resolutions. In our preliminary experiments, we found a higher f led to the majority of reconstructions being of an untenable quality. Conversely, decreasing f led to latent representations of sizes that resulted in large memory requirements in the downstream SUNDAE prior, making inference on consumer-grade GPUs impractical.

Training VQ-GAN at this resolution and at our chosen downsampling rate is extremely computationally expensive. This made a full hyperparameter sweep of VQ-GAN’s parameters not possible. Therefore, we accepted good reconstructions on average with occasional artifacts that could potentially manifest in the final samples. Improving the effectiveness of VQ image models is not the focus of this research project. We found these artifacts to only rarely appear in the final samples, shown in §4.1.

3.6 ARBITRARY PATTERN INPAINTING

As noted in the original work (Savinov et al., 2022) and other NAR solutions (Bond-Taylor et al., 2021a), one advantage of NAR models is that they are not limited to causal inpainting. They support arbitrary inpainting masks and draw upon context from \mathbf{z}_{t-1} , rather than $\mathbf{z}_{t-1}^{<i}$, enabling them to easily perform inpainting tasks that are complex to implement with AR models. This property also results in higher quality and more diverse samples (Bond-Taylor et al., 2021a).

The inpainting procedure takes an image $\mathbf{y} \in \mathbb{R}^{H \times W \times 3}$ and a pixel-level binary mask $m_p \in \{0, 1\}^{H \times W}$ as input. By taking $f \times f$ regions of m_p and applying a logical AND in them, we

obtain a latent level mask $m_{vq} \in \{0, 1\}^{h \times w}$. We encode \mathbf{x} using E to obtain \mathbf{z} , and then initialise our starting latent \mathbf{z}_0 by randomly setting points in \mathbf{z} where $m_{vq} = 1$, and keeping \mathbf{z} the same when $m_{vq} = 0$. We then sample starting from \mathbf{z}_0 , allowing the model full context, but only update regions that were masked according to m_{vq} . Though not strictly necessary, we use a lower temperature for inpainting ($0.3 \leq \tau \leq 0.5$) to bias sampling towards more confident choices, as more true context is available to the model. Decoding \mathbf{z}_T with G produces the final result \mathbf{y} , identical to the end of the sampling process.

Sampling at a latent level means the model is unable to do fine-grained inpainting at a pixel level. The definition of the VQ mask m_{vq} means that some pixels outside the mask may be altered if the pixel mask is not perfectly aligned with the VQ mask (when AND does not always receive all 0s or all 1s). We found in practise this had little effect on the perceptual quality of the outputs.

4 EVALUATION

4.1 UNCONDITIONAL IMAGE GENERATION



Figure 7: Unconditional FFHQ 1024×1024 samples generated in $T = 100$ sampling steps.

Model	FID	Density	Coverage
VQ-GAN + Transformer (Esser et al., 2021)	9.76	—	—
VQ-GAN + Absorbing DDPM Bond-Taylor et al. (2021a)	6.11	1.51	0.83
ViT-VQGAN + Transformer (Yu et al., 2021)	5.3	—	—
VQ-GAN + SUNDAE ($T = 200$)	11.79	0.72	0.21
VQ-GAN + SUNDAE ($T = 100$)	10.56	0.77	0.43

Table 1: Results on FFHQ 256×256 for unconditional image generation.

Model	FID	Density	Coverage
VQ-GAN + Transformer (Esser et al., 2021)	10.2	—	—
ViT-VQGAN + Transformer (Yu et al., 2021)	7.0	—	—
VQ-GAN + SUNDAE ($T = 200$)	21.25	0.40	0.33
VQ-GAN + SUNDAE ($T = 100$)	17.96	0.43	0.36

Table 2: Results on CelebA 256×256 for unconditional image generation.

We evaluate our method on the task of unconditional image generation using datasets FFHQ256, FFHQ1024, and CelebA. We evaluate our models using FID Infinity (Chong & Forsyth, 2020), coverage, and density (Naeem et al., 2020). Additionally, we show representative unconditional samples in Figures 1 & 7, with additional samples in Appendix B.2.

We present our results for the 256×256 image generation experiments in Table 1 and Table 2 for FFHQ and CelebA respectively. Though the samples for models trained on these datasets are of good quality, they do not improve upon prior work utilising VQ-GAN to generate images, in terms of our chosen perceptual quality metrics. However, our FID score for FFHQ256 falls close to the reported score in Esser et al. (2021) using less than half the number of sampling steps. Additionally, both Bond-Taylor et al. (2021a) and Yu et al. (2021) utilise improved VQ-GANs, whereas we use

the original formulation. This suggests that applying SUNDAE to these variants could improve our scores further.

For the megapixel experiments, samples shown in Figures 1 & 7 demonstrate that our model is capable of generating high quality and diverse samples. Our aim was to push the efficiency of generative models to their limit, however we were still surprised at precisely how fast the model could sample—particularly on megapixel scale experiments. The samples in Figure 1 were created in two seconds on a GTX 1080Ti. This can be further improved with more powerful accelerators and further optimisation. Additionally, our success here demonstrates the scalability of SUNDAE to sequence lengths of $N = 1024$, larger than the maximum length tested in the original work ($N = 256$) that proposed SUNDAE (Savinov et al., 2022).

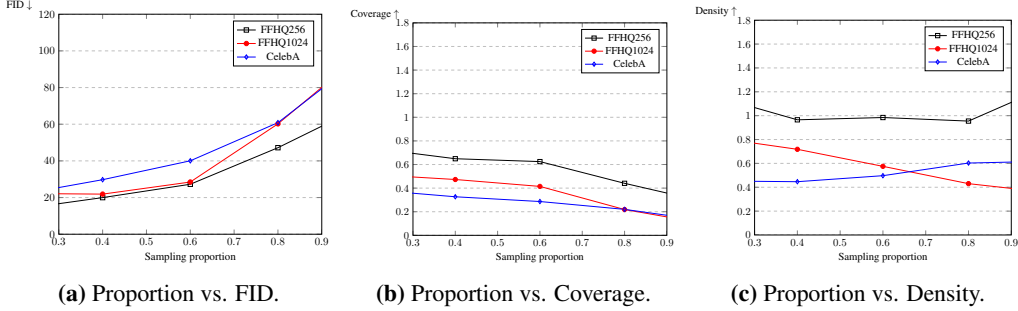


Figure 8: Plots showing sample quality in terms of different perceptual metrics as sample proportion is changed. Lower proportions perform better provided T is sufficiently high.

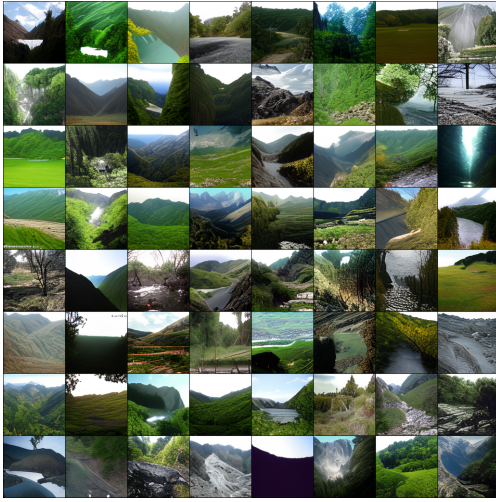
However, in terms of perceptual quality metrics, our approach again does not improve upon prior work, obtaining a FID score of 21.85, density of 0.77, and coverage of 0.47 using $T = 100$ sampling steps. This is likely due to being bottlenecked by our relatively weak VQ-GAN prior model. Further work is needed to improve the reconstruction quality of VQ-GAN on images at this resolution. It should be emphasized that an AR model learning the same FFHQ1024 prior would require $T = 1024$ sampling steps. Additionally, across all datasets, reasonable samples can be obtained in as few as $T = 50$ sampling steps, such as those in Figure 1, though sample quality is more inconsistent.

Table 8 shows that recommendations to prefer low proportion sampling not only holds for natural language tasks (Savinov et al., 2022) but also for the sampling of discrete latents. Across all datasets, the best FID and coverage scores were obtained with our minimum tested proportion of 0.2. It should be noted that this is only possible when a sufficient number of sampling steps is available to the model, else each individual position in \mathbf{z}_t will not have enough opportunities to update. Additionally, Table 1 and Table 2 show that naively increasing the number of sampling steps (without changing other parameters) does not necessarily lead to improved performance. Further work is needed to study best practises for adjusting other sample-time parameters when scaling the number of sampling steps.

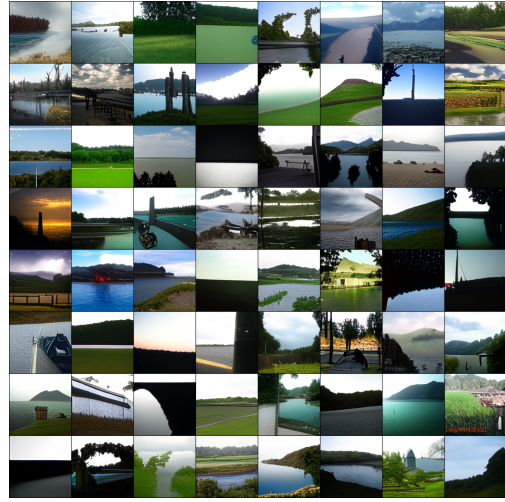
4.2 CLASS-CONDITIONED IMAGE GENERATION

Another critical component of an ideal generative model is the ability to control its generation. We explore class-conditioned image generation of ImageNet at 256×256 resolution, using pretrained ImageNet256 VQ-GAN checkpoints.

There are many valid ways of injecting a conditioning signal into generative models, for example passing one-hot or embedding class vectors. We use a simple solution proposed in Parmar et al. (2018): adding a learned class embedding to every input embedding. To test whether their proposed method can also be applied to SUNDAE, we conducted an experiment on discrete MNIST-style datasets. We treat each of the possible 8-bit greyscale colour values as a codebook index, resulting in $v = 256$ —generating pixels directly rather than image patches. Results of these experiments are shown in Figure 10 and demonstrate that SUNDAE can incorporate conditional information using this simple approach.



(a) 256×256 successful samples from the class “Valley”.



(b) 256×256 successful samples from the class “Lakeside”.



(c) 256×256 failed samples from the class “King Penguin”.



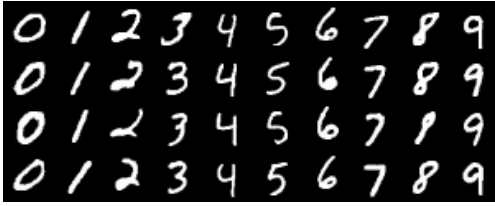
(d) 256×256 failed samples from the class “Giant Panda”.

Figure 9: Examples of class-conditioned generation on ImageNet256 using $T = 50$ sampling steps. Top row contains examples of successful samples whereas bottom row contains failed samples. The contents of the failed samples resemble the target class, but are of low quality.

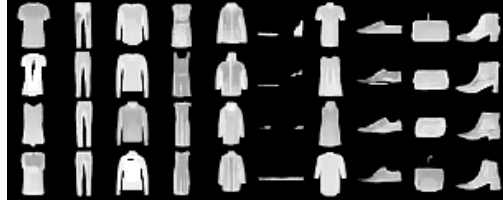
Despite this, our model fails to produce reasonable samples for all classes in ImageNet. On classes containing large scenes such as landscapes, the samples are convincing and diverse. However, for classes requiring fine-grained detail, the outputs merely resemble the target class. Results of conditional generation with four representative classes are shown in Figure 9. Due to this, we chose not to compute perceptual metrics for conditional experiments as the sample quality was clearly insufficient via inspection alone. This could be a result of lack of model capacity, lack of training time, or the conditioning strategy tested on MNIST being insufficient for ImageNet. The training of a more effective conditional model is left for future work.

4.3 ARBITRARY IMAGE INPAINTING

As outlined earlier, non-autoregressive generative models have a number of advantages for inpainting tasks, including supporting arbitrary masks and being able to use the full context available to



(a) Conditional generation on MNIST.

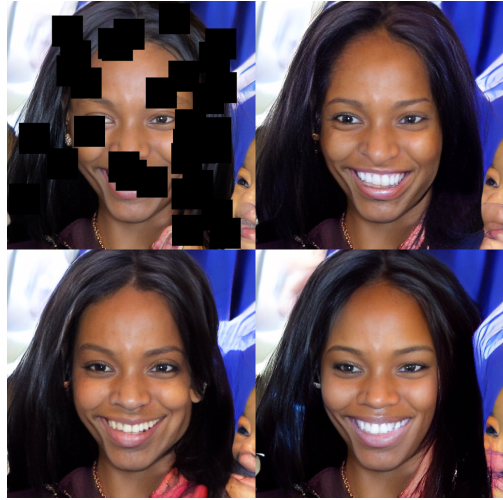


(b) Conditional generation on Fashion-MNIST.

Figure 10: Testing conditional generation using MNIST-style datasets. Coherent samples demonstrate that the proposed conditioning method does inject class information.



(a) Multiple results of inpainting using the same block mask.



(b) Multiple results of inpainting on the same random mask.

Figure 11: Inpainting results on FFHQ1024. We compute multiple outputs per input image and mask to demonstrate diversity of outputs.

them. We provide a number of examples of inpainting on FFHQ1024, showcasing different patterns and results given the same starting image and mask. As our method utilises a VQ image model, it is incapable of doing fine-grained inpainting at a pixel level. We found in practise this had little effect on the perceptual quality of the outputs, as shown in Figure 11.

4.4 LIMITATIONS

As a result of our evaluation, some limitations of our approach arise. One weakness is that our VQ image model utilises adversarial components within it. This potentially means that image patches (corresponding to each codebook entry) could suffer from mode collapse issues, which does indeed occur with certain hair textures. Additionally, we encountered consistent instability during training of the large VQ-GANs which resulted in many failed training runs. Further research into high compression VQ models that do not use adversarial components remains an open and challenging area of research. When such a VQ model is designed, it can easily be substituted into our proposed framework.

Despite our model demonstrating extremely fast sampling it falls short of many recent methods in terms of perceptual quality metrics. Though measures of perceptual quality such as FID are known to be flawed (Chong & Forsyth, 2020), other measures such as density and coverage also show inferior sample quality (Naeem et al., 2020). This is especially true on ImageNet where many classes merely resemble the target class—likely due to lack of model capacity and training time. Despite this, the resulting samples on the FFHQ and CelebA datasets are still very diverse and of good perceptual

quality. Further work, particularly extensive hyperparameter sweeps, is needed to improve quality in terms of these perceptual metrics.

5 CONCLUSION

In this work we investigated pushing the efficiency of generative models using a modified hourglass transformer and a non-autoregressive sampling method, following the trend in generative modelling research of simultaneously improving quality and speed of sampling using non-adversarial approaches. We found that the combination of these techniques formed a fast image generation framework. To our surprise, the proposed method was faster and more scaleable than expected, able to be applied with ease to megapixel images, and generate samples at such resolutions in seconds—considerably faster than existing non-adversarial methods. Additionally, we found that the performance of hourglass transformers on multidimensional data can be improved through adjustments to resampling and positional embedding mechanisms—applicable in any task applying hierarchical transformers to multidimensional data. We also demonstrated the scalability of SUNDAE by applying it to sequences of length 1024—longer than evaluated on in the original work. This demonstrates the superiority of the non-autoregressive paradigm, and joins a rapidly growing space of research into their use as a viable alternative to autoregressive frameworks. Additional research is needed into better VQ image models and into a stronger conditional generative model, as well as closing the gap between our proposed solution and existing models in terms of perceptual quality metrics.

ACKNOWLEDGMENTS

This work made use of the facilities of the N8 Centre of Excellence in Computationally Intensive Research (N8 CIR) provided and funded by the N8 research partnership and EPSRC (Grant No. EP/T022167/1). The Centre is co-ordinated by the Universities of Durham, Manchester and York.

In addition, this work has used Durham University’s NCC cluster. NCC has been purchased through Durham University’s strategic investment funds, and is installed and maintained by the Department of Computer Science.

REFERENCES

- Jacob Austin, Daniel D. Johnson, Jonathan Ho, Daniel Tarlow, and Rianne van den Berg. Structured denoising diffusion models in discrete state-spaces, 2021.
- Stella Biderman, Sid Black, Charles Foster, Leo Gao, Eric Hallahan, Horace He, Ben Wang, and Phil Wang. Rotary embeddings: A relative revolution. blog.eleuther.ai/, 2021. [Online; accessed].
- Sam Bond-Taylor, Peter Hesse, Hiroshi Sasaki, Toby P. Breckon, and Chris G. Willcocks. Unleashing transformers: Parallel token prediction with discrete absorbing diffusion for fast high-resolution image generation from vector-quantized codes, 2021a.
- Sam Bond-Taylor, Adam Leach, Yang Long, and Chris G. Willcocks. Deep generative modelling: A comparative review of vaes, gans, normalizing flows, energy-based and autoregressive models. *IEEE Transactions on Pattern Analysis and Machine Intelligence*, pp. 1–1, 2021b. ISSN 1939-3539. doi: 10.1109/tpami.2021.3116668. URL <http://dx.doi.org/10.1109/TPAMI.2021.3116668>.
- Xi Chen, Nikhil Mishra, Mostafa Rohaninejad, and Pieter Abbeel. Pixelsnail: An improved autoregressive generative model, 2017.
- Rewon Child, Scott Gray, Alec Radford, and Ilya Sutskever. Generating long sequences with sparse transformers. *arXiv preprint arXiv:1904.10509*, 2019.
- Kyunghyun Cho, Bart van Merriënboer, Dzmitry Bahdanau, and Yoshua Bengio. On the properties of neural machine translation: Encoder-decoder approaches, 2014.

-
- Min Jin Chong and David Forsyth. Effectively unbiased fid and inception score and where to find them. In *Proceedings of the IEEE/CVF conference on computer vision and pattern recognition*, pp. 6070–6079, 2020.
- Zihang Dai, Guokun Lai, Yiming Yang, and Quoc V. Le. Funnel-transformer: Filtering out sequential redundancy for efficient language processing, 2020.
- Jacob Devlin, Ming-Wei Chang, Kenton Lee, and Kristina Toutanova. Bert: Pre-training of deep bidirectional transformers for language understanding, 2019.
- Laurent Dinh, David Krueger, and Yoshua Bengio. Nice: Non-linear independent components estimation. *arXiv preprint arXiv:1410.8516*, 2014.
- Patrick Esser, Robin Rombach, and Björn Ommer. Taming transformers for high-resolution image synthesis, 2021.
- Ian J. Goodfellow, Jean Pouget-Abadie, Mehdi Mirza, Bing Xu, David Warde-Farley, Sherjil Ozair, Aaron Courville, and Yoshua Bengio. Generative adversarial networks, 2014.
- Jonathan Ho, Ajay Jain, and Pieter Abbeel. Denoising diffusion probabilistic models, 2020.
- Sepp Hochreiter and Jürgen Schmidhuber. Long short-term memory. *Neural Computation*, 9(8): 1735–1780, 1997.
- Emiel Hooeboom, Alexey A Gritsenko, Jasmijn Bastings, Ben Poole, Rianne van den Berg, and Tim Salimans. Autoregressive diffusion models. *arXiv preprint arXiv:2110.02037*, 2021.
- Diederik P Kingma and Jimmy Ba. Adam: A method for stochastic optimization. *arXiv preprint arXiv:1412.6980*, 2014.
- Diederik P Kingma and Max Welling. Auto-encoding variational bayes, 2013.
- Muhammad Ferjad Naeem, Seong Joon Oh, Youngjung Uh, Yunje Choi, and Jaejun Yoo. Reliable fidelity and diversity metrics for generative models. *International Conference on Machine Learning*, 2020.
- Piotr Nawrot, Szymon Tworkowski, Michał Tyrolski, Łukasz Kaiser, Yuhuai Wu, Christian Szegedy, and Henryk Michalewski. Hierarchical transformers are more efficient language models, 2021.
- Niki Parmar, Ashish Vaswani, Jakob Uszkoreit, Łukasz Kaiser, Noam Shazeer, Alexander Ku, and Dustin Tran. Image transformer, 2018.
- Adam Paszke, Sam Gross, Francisco Massa, Adam Lerer, James Bradbury, Gregory Chanan, Trevor Killeen, Zeming Lin, Natalia Gimelshein, Luca Antiga, Alban Desmaison, Andreas Kopf, Edward Yang, Zachary DeVito, Martin Raison, Alykhan Tejani, Sasank Chilamkurthy, Benoit Steiner, Lu Fang, Junjie Bai, and Soumith Chintala. Pytorch: An imperative style, high-performance deep learning library. In H. Wallach, H. Larochelle, A. Beygelzimer, F. d’Alché-Buc, E. Fox, and R. Garnett (eds.), *Advances in Neural Information Processing Systems 32*, pp. 8024–8035. Curran Associates, Inc., 2019. URL <http://papers.neurips.cc/paper/9015-pytorch-an-imperative-style-high-performance-deep-learning-library.pdf>.
- Aditya Ramesh, Mikhail Pavlov, Gabriel Goh, Scott Gray, Chelsea Voss, Alec Radford, Mark Chen, and Ilya Sutskever. Zero-shot text-to-image generation, 2021.
- Nikolay Savinov, Junyoung Chung, Mikolaj Binkowski, Erich Elsen, and Aaron van den Oord. Step-unrolled denoising autoencoders for text generation, 2022.
- Yang Song and Stefano Ermon. Generative modeling by estimating gradients of the data distribution, 2019.
- Jianlin Su, Yu Lu, Shengfeng Pan, Bo Wen, and Yunfeng Liu. Roformer: Enhanced transformer with rotary position embedding, 2021.

Aaron van den Oord, Nal Kalchbrenner, and Koray Kavukcuoglu. Pixel recurrent neural networks, 2016.

Aaron van den Oord, Oriol Vinyals, and Koray Kavukcuoglu. Neural discrete representation learning, 2017.

Aaron van den Oord, Oriol Vinyals, and Koray Kavukcuoglu. Neural discrete representation learning, 2018.

Ashish Vaswani, Noam Shazeer, Niki Parmar, Jakob Uszkoreit, Llion Jones, Aidan N. Gomez, Lukasz Kaiser, and Illia Polosukhin. Attention is all you need, 2017.

Alex Wang and Kyunghyun Cho. Bert has a mouth, and it must speak: Bert as a markov random field language model, 2019.

Zhisheng Xiao, Karsten Kreis, and Arash Vahdat. Tackling the generative learning trilemma with denoising diffusion gans, 2021.

Yunyang Xiong, Zhanpeng Zeng, Rudrasis Chakraborty, Mingxing Tan, Glenn Fung, Yin Li, and Vikas Singh. Nystromformer: A nystrom-based algorithm for approximating self-attention. In *Proceedings of the... AAAI Conference on Artificial Intelligence. AAAI Conference on Artificial Intelligence*, volume 35, pp. 14138. NIH Public Access, 2021.

Jiahui Yu, Xin Li, Jing Yu Koh, Han Zhang, Ruoming Pang, James Qin, Alexander Ku, Yuanzhong Xu, Jason Baldridge, and Yonghui Wu. Vector-quantized image modeling with improved vqgan, 2021.

A IMPLEMENTATION DETAILS

A.1 SUNDAE IMPLEMENTATION

Dataset	FFHQ256	FFHQ1024	CelebA	MNIST	FashionMNIST	ImageNet
Dataset Size	60,000	60,000	30,000	60,000	60,000	1.28M
Codebook Size	1024	8192	1024	256	256	1024
Latent Shape	16×16	32×32	16×16	28×28	28×28	16×16
Unroll Steps	3	3	3	2	2	3
Depth	3 – 16 – 3	2 – 12 – 2	2 – 12 – 2	2 – 8 – 2	2 – 8 – 2	3 – 14 – 3
Dimension	1024	1024	1024	1024	1024	1024
Shorten Factor	4	4	4	4	4	4
Attention Heads	8	8	8	8	8	12
Resample Type	Linear	Linear	Linear	Linear	Linear	Linear
Classes	—	—	—	10	10	1000
Class Dimension	—	—	—	1024	1024	1024

Table 3: Table of parameters for all training experiments. Depth is represented as three numbers corresponding to number of layers before downsampling, number of downsampled layers, and number of layers after upsampling. The dataset size is the size of the training split of the dataset. The latent shape of MNIST experiments is exactly equal to the shape of \mathbf{x} , as for these experiments we operate directly on a (discrete) pixels.

All SUNDAE models are trained using the *Adam* optimizer (Kingma & Ba, 2014) as realised in its *AdamW* implementation in PyTorch (Paszke et al., 2019). All models and training scripts are implemented in PyTorch, trained on a single 80 GiB Nvidia A100. Similarly, computation of perceptual scores such as FID was done on this same device. Inference for all models can be run on a consumer-grade GPU, in our case a Nvidia GTX 1080Ti. All parameters used for training the SUNDAE models are shown in Table 3.

A.2 VQ-GAN IMPLEMENTATION

Codeword Dimension	256
Number of Codewords	8192
Encoder Channels	[128, 128, 256, 256, 512, 512]
Downsampling Rate f	32
Number of Residual Blocks	1
Attention Resolution	≤ 64
Dropout	0.0
Discriminator Start	15000
Number of Discriminator Layers	3
Discriminator Weight	0.5
Codebook Weight	1.0
Local Batch Size	1
Global Batch Size	4

Table 4: Table of parameters for VQ-GAN training at 1024×1024 resolution.

Where possible, we used pretrained VQ-GAN checkpoints provided by Esser et al. (2021), who originally introduced VQ-GAN. For FFHQ1024 experiments, we trained our own VQ-GAN using training scripts provided by Esser et al. (2021) on four 32 GiB Nvidia V100 GPUs. The chosen hyperparameters for VQ-GAN for this task is shown in Table 4.

B ADDITIONAL RESULTS

B.1 EFFECT OF SAMPLING HYPERPARAMETERS

This section shows a non-comprehensive overview of the effect of varying sample-time hyperparameters on image quality.

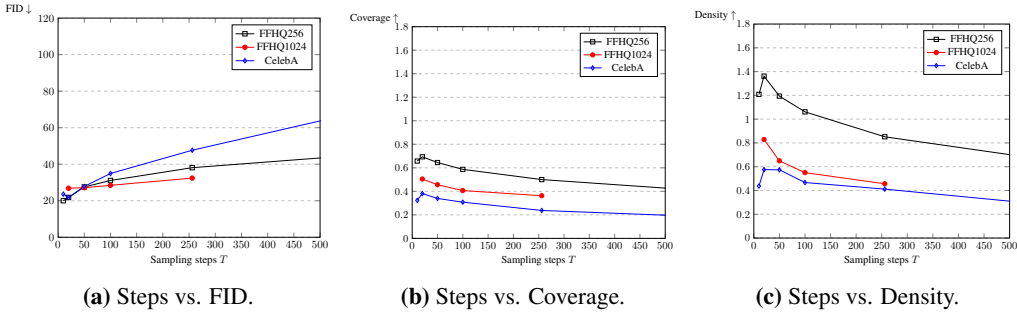


Figure 12: Plots showing sample quality in terms of different metrics as number of sampling steps T increases. Counter-intuitively, the sample quality decreases with number of sampling steps, seen on all metrics and datasets. This indicates that naively scaling the number of sampling steps (without adjusting number of parameters) does not necessarily improve results.

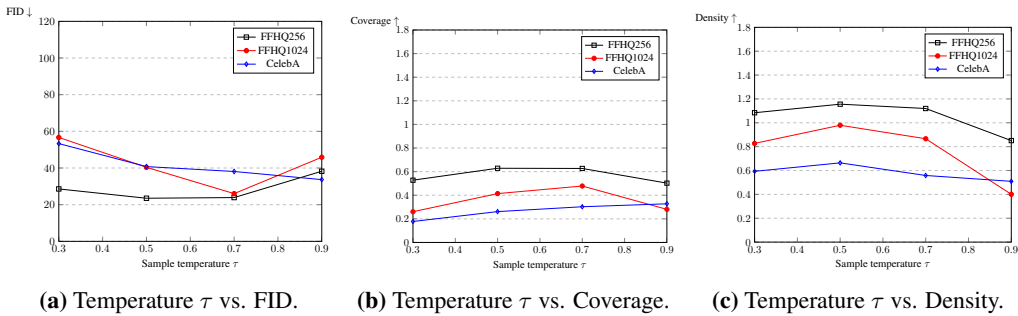


Figure 13: Plots showing sample quality in terms of different metrics as sample temperature τ is changed. Given the other parameters, a good choice of τ falls in the range 0.5 – 0.7. However, this range may differ depending on the values of other parameters, and naturally higher temperatures lead to more diverse samples.

B.2 UNCONDITIONAL SAMPLES



Figure 14: Unconditional FFHQ 1024×1024 samples generated in $T = 100$ sampling steps.

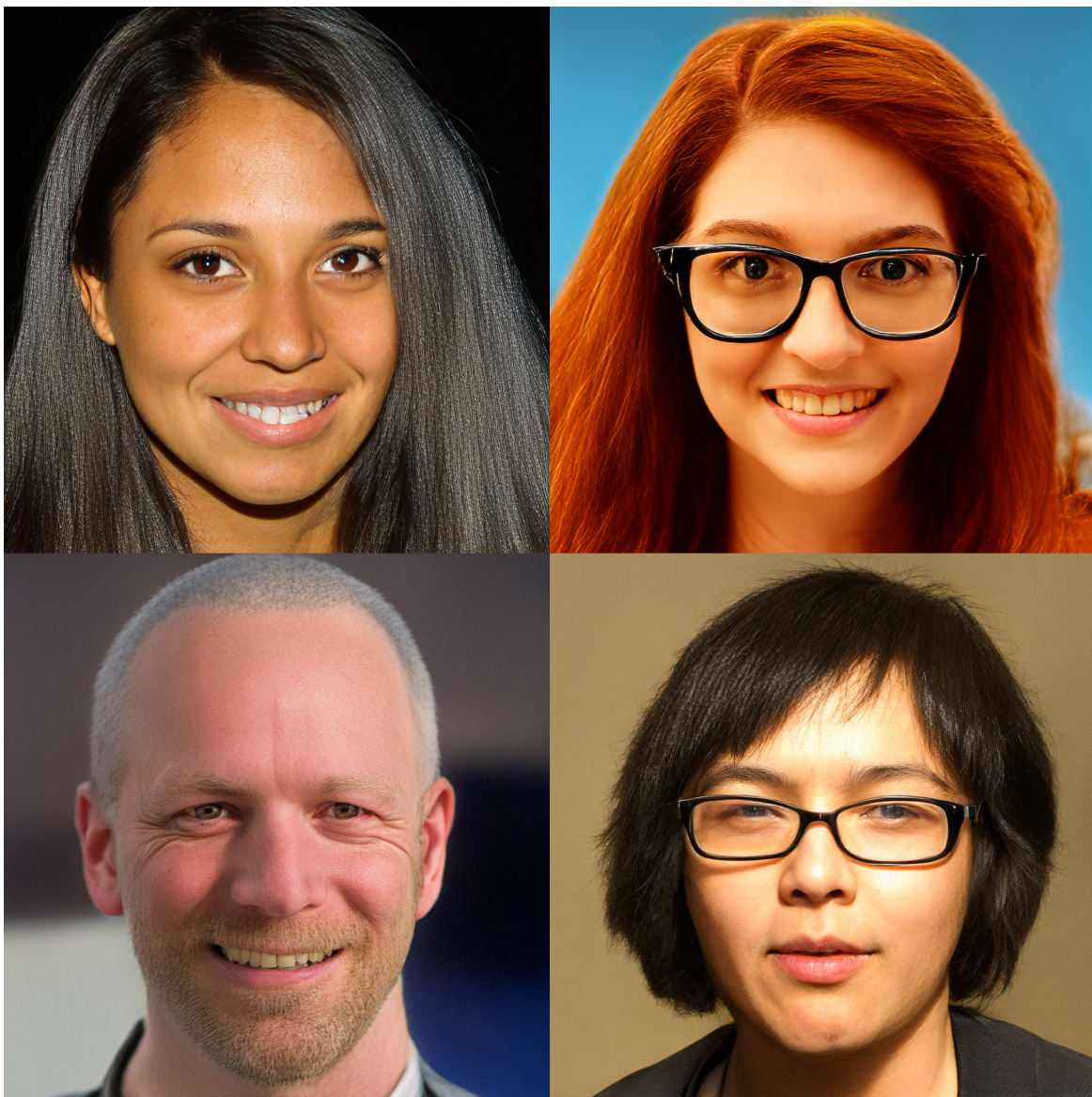


Figure 15: Unconditional FFHQ 1024×1024 samples generated in $T = 100$ sampling steps.

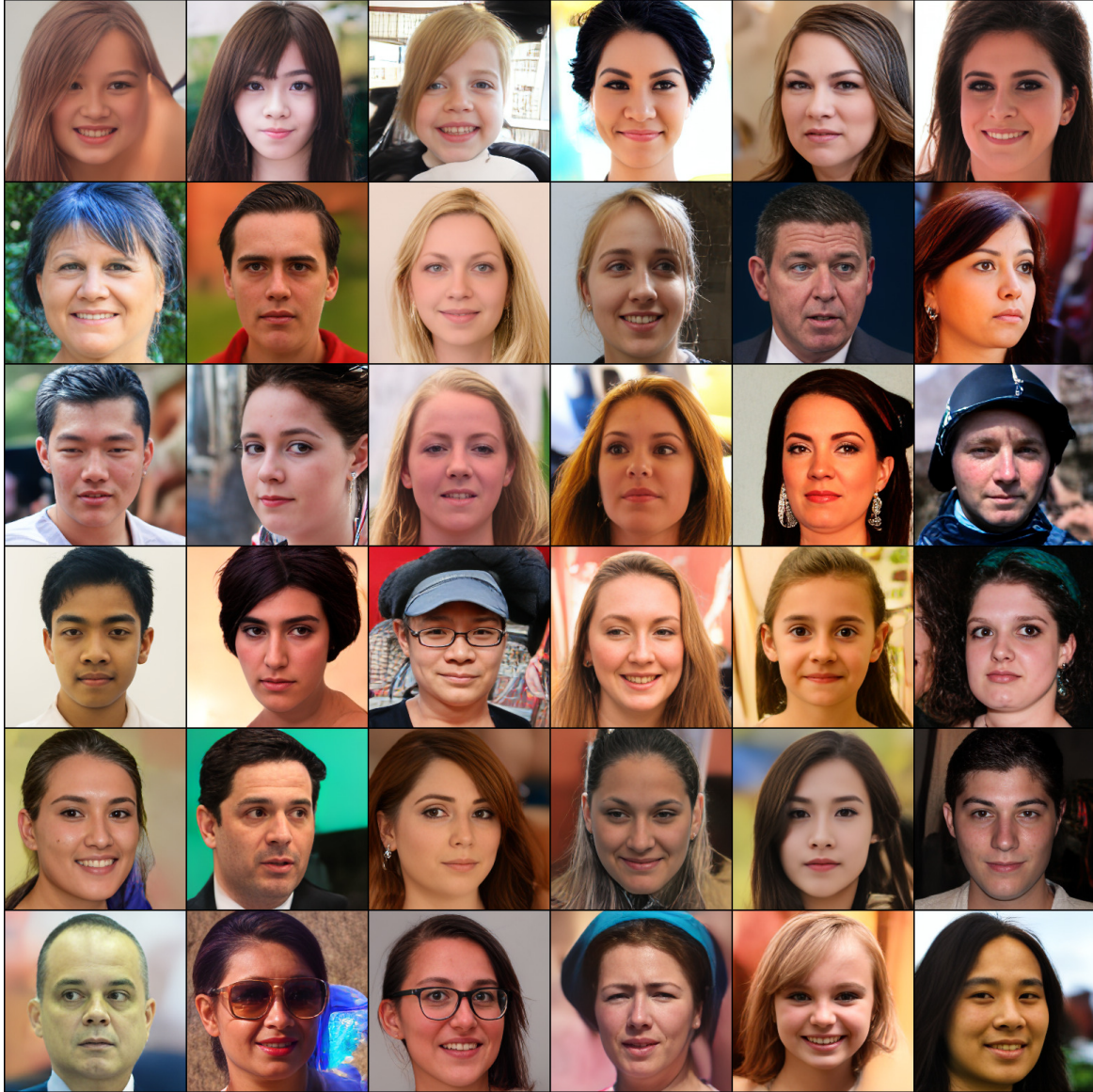


Figure 16: Unconditional FFHQ 256×256 samples generated in $T = 50$ sampling steps.



Figure 17: Unconditional FFHQ 256×256 samples generated in $T = 100$ sampling steps.



Figure 18: Unconditional CelebA 256×256 samples generated in $T = 50$ sampling steps.



Figure 19: Unconditional CelebA 256×256 samples generated in $T = 100$ sampling steps.

B.3 IMAGE INPAINTING



Figure 20: Large example of inpainting at 1024×1024 resolution using FFHQ model.